 doi:10.20944/preprints202102.0245.v1

# Synthesis and Characterization of Silver–Strontium (Ag-Sr) Doped Mesoporous Bioactive Glass Nanoparticles

Shaher Bano[1], Memoona Akhtar[1], Muhammad Yasir[1], Muhammad Salman Maqbool[2], Akbar Niaz[3], Abdul Wadood[1], Muhammad Atiq Ur Rehman[1*]

[1]*Department of Materials Science and Engineering, Institute of Space Technology Islamabad, Islamabad 44000, Pakistan*

[2] *Department of Mechanical and Manufacturing Engineering, La Trobe University, Melbourne VIC 3086, Australia*

[3] Department of Mechanical Engineering, *King Faisal University, Al Hufūf, Saudi Arabia*

**corresponding author: atique1.1@hotmail.com (muhammad.atiq@mail.ist.edu.pk)*

## Abstract

Biomedical implants are the need of this era due to the increase in number of accidents and follow-up surgeries. Different types of bone diseases such as osteoarthritis, osteomalacia, bone cancer, etc. are increasing globally. Mesoporous bioactive glass nanoparticles (MBGNs) are used in biomedical devices due to their osteointegration and bioactive properties. In this study, silver (Ag) and strontium (Sr) doped mesoporous bioactive glass nanoparticles (Ag-Sr MBGNs) were prepared by a modified Stöber process. In this method, $Ag^{+}$ & $Sr^{2+}$ were co-substituted in pure MBGNs to harvest the antibacterial properties of Ag ions, as well as pro-osteogenic potential of $Sr^{2}$ ions. The effect of the two ion concentration on morphology, surface charge, composition, antibacterial ability, and in-vitro bioactivity was studied. Scanning electron microscopy (SEM), X-Ray diffraction (XRD) and Fourier transform infrared spectroscopy (FTIR) confirmed the doping of Sr and Ag in MBGNs. SEM and EDX analysis confirmed the spherical morphology and typical composition of MBGNs, respectively. The Ag-Sr MBGNs showed a strong antibacterial effect against Staphylococcus carnosus and Escherichia coli bacteria determined via turbidity and disc diffusion method. Moreover, the synthesized Ag-Sr MBGNs develop apatite-like crystals upon immersion in simulated body fluid (SBF), which suggested that the addition of Sr improved in-vitro bioactivity. The Ag-Sr MBGNs synthesize in this study can

 doi:10.20944/preprints202102.0245.v1

be used for the preparation of scaffolds or as a filler material in the composite coatings for bone tissue engineering.

**Keywords:** Mesoporous Bioactive Glass Nanoparticles; Sol-Gel; Antibacterial Activity; Silver; Bioactivity

## 1. Introduction

Millions of medical devices are being implanted nowadays into patients related to bone diseases and accidental surgeries, thanks to the advancement of biomaterials. During the last few decades, biomaterials have focused on the following issues: (a) establish a material with a suitable mechanical strength, (b) improve in-vitro activity by increasing the surface area of the bioceramics [1,2]. The number of accidents worldwide are increasing periodically. Moreover, the percentage of people over 50 years are suffering from diseases like osteoporosis, osteoarthritis, osteomalacia, bone cancer and other musculoskeletal diseases [3]. It is stated that only in the USA annually more than 500,000 primary arthroplasties including total joint replacement, total hip arthroplasty(THA), total knee arthroplasty (TKA) are done, and more than 1.3 million people live with artificial joints [4].

These problems are being solved by permanent replacement of the bones or by temporary biodegradable devices. However, a bio implant may fail during service resulting in aseptic bio-mechanical loosening, followed by prosthetic joint infection [5–7]. Thus, patients need to go through revisionary surgeries. A study quoted that 312 out of 402 patients (around 78%) had to go through revisionary surgery after total knee arthroplasty (TKA) between January 2010 and December 2015 [8]. Infection of bone tissues is essentially caused by microorganisms, most commonly by gram-positive (Staphylococcus aureus and Staphylococcus epidermidis) and gram-negative bacteria (Escherichia Coli) [9]. These bacteria can reach the infectious surface either through the bloodstream, by extension from the local environment, surgical equipment, or may already be present in patient's body or skin. Biofilm formation takes place in several stages. Firstly, bacterial cells rapidly attach with the surface of the implant, secondly micro colonies of the multilayered structured are formed and excrete extracellular polymeric substance(EPS). In the third step, cells mature and form multi-layered clusters and bio film is formed. Fourth step is followed by three-dimensional growth of biofilm that act as barrier for antibiotics as well as host

Preprints (www.preprints.org) | NOT PEER-REVIEWED | Posted: 10 February 2021 doi:10.20944/preprints202102.0245.v1

defense mechanism. At last critical mass of biofilm is achieved and its starts colonization on other surfaces [9].

To prevent revisionary surgeries of orthopedic implants, the implant material must be livable to form bone-forming tissues, delay or inhibit the formation of soft connective tissues, and depress bacterial adherence [10–12]. After the discovery of Bio glass® (BG) by Professor Larry L. Hench in 1969, the concept of biocompatibility extended [13]. This concept is always a driving force for the discovery of new biomaterials that have good mechanical properties or acceptable bone bond strength. With respect to their development, the biomaterials can be broadly classified into 3 groups. First generation biomaterials fulfilled the requirement of mechanical strength, and had acceptable physical properties. However, they were biologically inert and, in some cases, the toxicity of these materials resulted in the implant failure [14]. Second generation materials were also bio-inert with a few exceptions involving surface modifications with bioactive ceramics. These coatings lead to a rapid reaction involving the ionic dissolution of silicon (Si), calcium (Ca), sodium (Na) and phosphorous (P), which are responsible for both extracellular and intracellular bioactivities at the implant-bone tissue interface. Second generation materials included ceramics (bioactive glass, glass–ceramics and calcium phosphates) and polymers (polyglycolide (PGA), polylactide (PLA). The concept of bioactivity further extended in third generation biomaterials in combination with biodegradability [13,15]. This class of biomaterials are being modified in the form of macroporous foams, composites which are bioresorbable and trigger regeneration of living tissues by activating genes. Third-generation bioactive glasses, composites, hybrid materials and macroporous foams are being designed to activate genes that stimulate regeneration of living tissues [16,17].

Furthermore, the concept of the mesoporous structure was introduced to enhance biocompatibility, ion release, and drug delivery. In this regard, pioneered BG was melt derived and closely related to the release of $Na^{+}$ and $Ca^{+2}$ ions for the deposition of the hydroxyapatite layer. Studies have shown that the release of $Ca^{+2}$ and $Si^{+2}$ from BG primarily stimulate the osteoblast proliferation [18]. However, this material inherited some limitations including required melting at a very high temperature (more than 1300 $^{\circ}$C), and less surface area due to the absence of porous structure [19]. On the other hand, mesoporous silica have pores in the range of 2 – 50 nm which increase the surface area, and serve as a channel for adsorption/desorption of drugs for targeted drug delivery

Preprints (www.preprints.org) | NOT PEER-REVIEWED | Posted: 10 February 2021 doi:10.20944/preprints202102.0245.v1

system [20–22]. Moreover, the therapeutic release of antibacterial and bioactive ions is anticipated to inhibit biofilm formation and resultant agony from infection, which is the main objective of this research work [21,23–27].

The research work presented in this study involves the synthesis and characterization of novel Ag and Sr-containing mesoporous bioactive glass nanoparticles (Ag-Sr-MBGNs) via a modified Stöber process [28]. Mesoporous bioactive glass nanoparticles were initially doped with various concentrations of Sr-Ag (5:1) mole %. Preliminary in-vitro bioactivity studies confirmed the suitability of Ag-Sr-MBGNs for bone tissue engineering applications, through formation of hydroxyapatite crystals upon immersion in simulated body fluid (SBF). The controlled release of Ag-Sr ions also induced the antibacterial characteristics without affecting the bioactivity of MBGNs. The antibacterial effect correlates with the release of metallic ions in a critical concentration of ions (Ag) which works against the relevant pathogen or bacteria in physiological conditions. Therefore, the results presented in this article are anticipated to be for a way forward in development of third generation biomaterials with the application of Ag-Sr-based MBGNs for scaffold fabrication as well as antibacterial coatings on metallic substrates. Not only osteogenic properties of other ions like (Cu, Mn & Zn) as well as their antibacterial studies have also been studied & their cytotoxic effects are also highlighted in literature[21]

## 2. Materials and Methods

### 2.1. Materials

Tetraethyl orthosilicate [TEOS]–99% (Sigma), calcium nitrate [Ca $(NO_3)_2$.4H2O] -98% (Sigma), silver nitrate [Ag $(NO_3)_2$]-99%(Sigma), strontium nitrate [Sr $(NO_3)_2$]-99%(Sigma), were used as silicon, calcium, silver and strontium sources, respectively. Furthermore, ethyl acetate 99.8% (Sigma), cetyltrimethylammonium bromide [CTAB]- 98%(Merck), ammonium hydroxide-35% (VWR, China), distilled water, and absolute ethanol- 99.8% were used. All chemicals used were of Analytical grade and American Chemical Society (ACS) grade.

### 2.2. Synthesis of Ag-Sr containing MBGNs (Stober Process)

Ag-Sr MBGNs were prepared by a modified Stöber process [29,30]. Firstly, 0.56 g CTAB was dissolved in 26 ml of distilled water under continuous stirring for 30 minute at $40^0$ C. Then, 8 ml ethyl acetate was added dropwise into the solution. Thirdly, dilute solution of ammonium

Preprints (www.preprints.org) | NOT PEER-REVIEWED | Posted: 10 February 2021 doi:10.20944/preprints202102.0245.v1

hydroxide (32%) was added to maintain pH at 9.5 and 3 ml of TEOS and was added dropwise into the above solution under continuous stirring. Finally, calcium nitrate, silver nitrate, and strontium nitrate was added depending upon the required composition and followed by magnetic stirring for 30 min. Afterwards, the solution was allowed to pursue reaction between the reactants. Subsequently, the suspension was centrifuged at 7830 rpm for 10 min to separate particles from the parent solution, followed by washing the sedimented particles with ethanol. This step was repeated three times. Finally, the precipitates were dried in an oven at 75 °C for 12 hours, followed by calcination at 700 °C for 5 hours. Figure 1 illustrates the synthesis of Ag-Sr doped MBGNs.

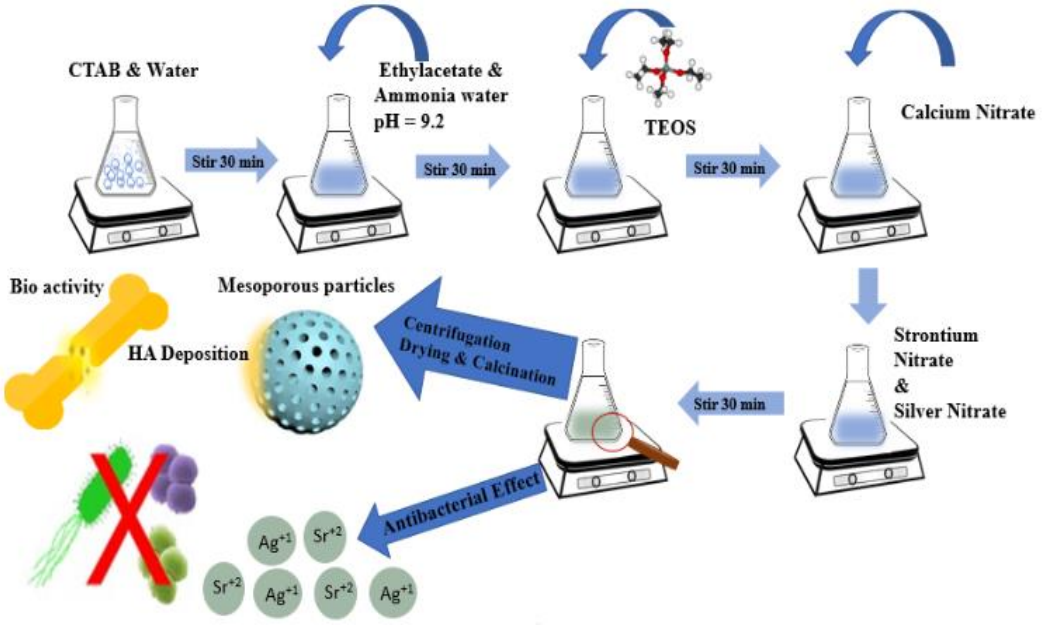


Figure1. Synthesis of Ag-Sr doped MBGNs modified by the Stöber method.

In this study, MBGNs with three different compositions were synthesize i.e., MBGNs doped with; 5 mol% Sr (5Sr-MBGNs), 1 mol% Ag (1Ag-MBGNs), and 5 mol% Sr and 1 mol% Ag (5Sr-1Ag MBGNs). Table 1illustrates the nominal composition of the synthesized MBGNs

Table1. Nominal composition of as-synthesized MBGNs

| Mesoporous bioactive glass nanoparticles type | Composition (mol%) | | | |
|---|---|---|---|---|
| | $SiO_2$ | CaO | SrO | AgO |
| MBGNs | 70 | 30 | 0 | 0 |
| 5Sr-MBGNs | 70 | 25 | 5 | 0 |
| 1Ag-MBGNs | 70 | 29 | 0 | 1 |
| 5Sr- 1Ag MBGNs | 70 | 24 | 5 | 1 |

Preprints (www.preprints.org) | NOT PEER-REVIEWED | Posted: 10 February 2021 doi:10.20944/preprints202102.0245.v1

### 2.3. Characterization of Ag-Sr Doped MBGNs

#### 2.3.1. Morphological Characterization

The surface morphology of the as-prepared nanoparticles as well as those obtained after bioactivity tests was investigated using scanning electron microscopy (SEM; LEO 435VP, Carl Zeiss™ AG). First, to make the samples conductive and reduce the effect of charging, the samples were coated with a thin layer (around 10 nm) of gold via sputtering technique (Q150/S, Quorum Technologies™). The SEM images were taken at different magnifications.

To further investigate the morphology of MBGNs, the specific surface area of MBGNs, Ag, Sr, Ag-Sr doped MBGNs was calculated via the BET (Brunauer−Emmett−Teller) method using the nitrogen desorption branch of the isotherm at -196 °C. Nitrogen adsorption/desorption was also used to measure the pore volume (porosity).

#### 2.3.2. Compositional Analysis

Energy-dispersive X-ray Spectroscopy (EDX, X-MaxN Oxford Instruments, Abingdon, UK ) was used to determine the composition of the as-synthesized particles. Furthermore, the ratio of the different elements in the hybrid nanoparticles was evaluated.

Fourier transform infrared spectroscopy (FTIR) measurements were carried out on pellets of Ag-Sr, Ag, and Sr doped MBGNs using potassium bromide (KBr) disk method on a Shimadzu IRAffinity-1S (Shimadzu Corp), equipped with Lab Solution IR software and a Quest ATR GS10801-B single bounce diamond accessory (Specac Ltd) at room temperature. In order to prepare samples for FTIR studies, the MBGNs were grounded to a fine powder, followed by mixing with KBr powder in the MBGNs: KBr ratio of 1:100. The mixture was subjected to further grinding to achieve a homogeneous mixture, followed by pressing using a hydraulic pressure of 5 tons/$cm^2$ to form the disk samples. The IR transmission spectra were recorded immediately after preparing the discs. For optimal results, the device was cleaned with ethanol before the sample was applied. Furthermore, a background scan was conducted with 128 runs. Every sample was measured with 128 transmittance scans with a resolution of 4 $cm^{-1}$ in Happ-Genzel apodization

Preprints (www.preprints.org) | NOT PEER-REVIEWED | Posted: 10 February 2021 doi:10.20944/preprints202102.0245.v1

using wavelengths from 400 - 4000 $cm^{-1}$. To reduce the signal noise, the spectra were smoothed by 15 points.

In addition to FTIR, the samples of Ag-Sr doped MBGNs were tested with X-Ray Diffraction (XRD) (MiniFlex 600, Rigaku Corporation, Europe) to characterize the doped MBGNs and pure MBGNs. The diffraction pattern was recorded using Ni-filtered Cu $K_\alpha$ radiation ($\lambda$ = 1.54 Å) operated at 40 kV and 40 mA over the 2$\theta$ angular range of 20-80° (with 0.02° step and a speed of 2° per minute).

### 2.3.1 Zeta potential

To measure the zeta potential, the Zetasizer Nano zsp (Malvern Panalytical GmbH) was used. The analyzed suspensions (powder samples in absolute ethanol) were diluted to the ratio of 0.1 $g.L^{-1}$ in particles. Three measurements per suspension at standard pH were taken at a maximum of 100 runs each and averaged. After each measurement, the cell was flushed out with ethanol again.

### 2.3.3. Ion-release Profile

To investigate the Ag and Sr ion release from prepared Ag-Sr MBGNs, 75 mg of powder sample was dispersed in SBF solution (50 mL) for different time intervals (day 1, day 3, day 7, day 14, and day 21) in an orbital shaking incubator at 37 °C. Ag and Sr ions released in the medium under dynamic conditions were measured, using ICP-OES (Inductively coupled plasma/optical emission spectrometry) from IRIS Advantage, Thermo Jarrell Ash. Approximately 1 g of the sample was dissolved in a 5% $HNO_3$ solution and heated gently to ensure complete dissolution. The solution was made up to 50 mL volumetrically and analyzed by ICP-OES (IRIS Advantage, Thermo Jarrell Ash) against a calibration traceable under ISO: 17025 guidance.

### 2.3.4. Antibacterial Studies

To test the antimicrobial properties of synthesized particles, an antibacterial test (called turbidity test) was conducted [27][28]. To grow E. coli and S. Carnasous bacteria in test tubes, a sterile wooden tip was used to scratch bacteria from a frozen sample and dropped into Lysogeny broth (LB-medium). After an incubation of 24 hours the medium had a high concentration of bacteria and was ready to use. Ag-Sr MBGNs, Ag MBGNs, Sr MBGNs, and Ag-Sr MBGNs were added in the test tubes and incubated for 24 hours. Then an optical density

Preprints (www.preprints.org) | NOT PEER-REVIEWED | Posted: 10 February 2021 doi:10.20944/preprints202102.0245.v1

measurement was performed with absorbance at 600 nm ($OD_{600}$). For each measurement, $OD_{600}$ medium was taken as a reference.

### 2.3.5. Disc Diffusion Test

Petri dishes were spread homogenously with heated agar inoculated with bacteria (E. coli and S. Carnasous). Afterwards, the prepared pellets of different concentrations of MBGNs were placed and then incubated at 37° C for 24h. After 24 h of incubation the petri dishes were taken out and digital images were taken to track the zone of incubation.

### 2.3.6. In-vitro Bioactivity Test

In-vitro bioactivity of the synthesized Ag-Sr MBGNs was investigated following Kokubo et al [33]. The synthesized Ag-Sr MBGNs was pressed into the pellets by using electrohydraulic pressing device (Mauthe Maschinenbau, Germany). The prepared pellets were immersed in SBF, the volume of SBF was set to 1 mg/ml. The SBF solution was changed every three days to simulate a refreshing system. The different sets of samples were taken after 1, 7, and 30 days. The samples were gently washed with DI-water to prevent salt crystals on the surface and put into the heating stove at 60 ℃ for drying. After drying, the samples were weighed for the degradation studies and characterized using SEM and EDX analysis.

## 3. Results and Discussion

### 3.1. Morphological Characterization

The morphology of the synthesized MBGNs was investigated by SEM analysis. Figure 2 shows that all types of MBGNs have spherical morphology regardless of the addition of metallic precursor. Figure 2 depicts that average particle size of synthesized MBGNs was 130 ± 15 nm. The microemulsion assisted sol–gel method favors the dispersion of nanoparticles which explains the homogeneous size and shape of the obtained nanoparticles [34].

Preprints (www.preprints.org) | NOT PEER-REVIEWED | Posted: 10 February 2021 doi:10.20944/preprints202102.0245.v1

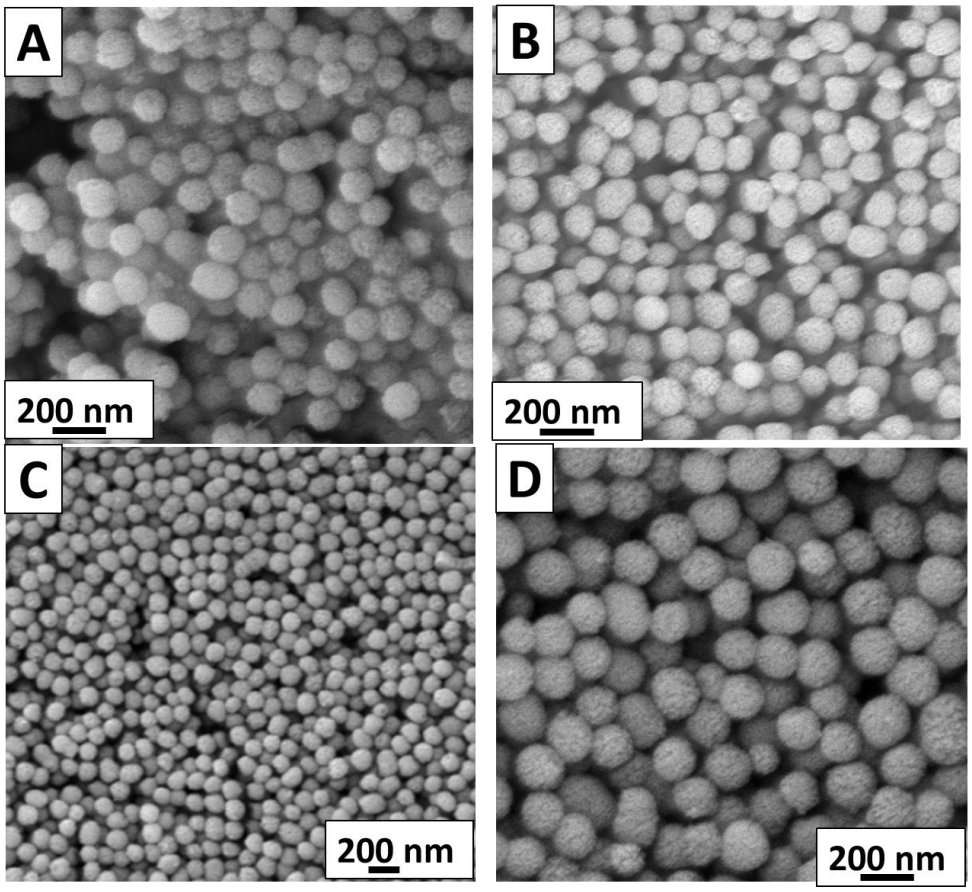


Figure 2. SEM images showing the morphology of the produced nanoparticles; (A) pure MBGNs (B) Ag – MBGNs (C) Sr-MBGNs (D) Ag-Sr MBGNs

The specific surface area of Sr, Ag, and Ag-Sr doped MBGNs was calculated via the Brunauer−Emmett−Teller (BET) method using the nitrogen desorption branch of the isotherm. Figure 3 depicts the pore size distribution of nitrogen adsorption-desorption isotherms of synthesized bioactive glass nanoparticles. Textural properties of Ag, Sr, and Ag-Sr MBGNs derived from nitrogen adsorption-desorption iso-therm analysis depicts type IV isotherm according to IUPAC which confirms the mesoporous structure [27]. Uptake of a high amount of nitrogen at P/Po ≈ 0.99 indicates the nano-sized particles. Figure 3 shows sharp nitrogen uptake from 0.40 to 0.60, which indicates the mesoporous character of particles (4-10 nm). Relatively high porosity in the synthesized MBGNs is responsible for the high surface area [35]. This porous nature opens up other biomedical applications such as drug delivery and microbial cell encapsulation [26].

Preprints (www.preprints.org) | NOT PEER-REVIEWED | Posted: 10 February 2021 doi:10.20944/preprints202102.0245.v1

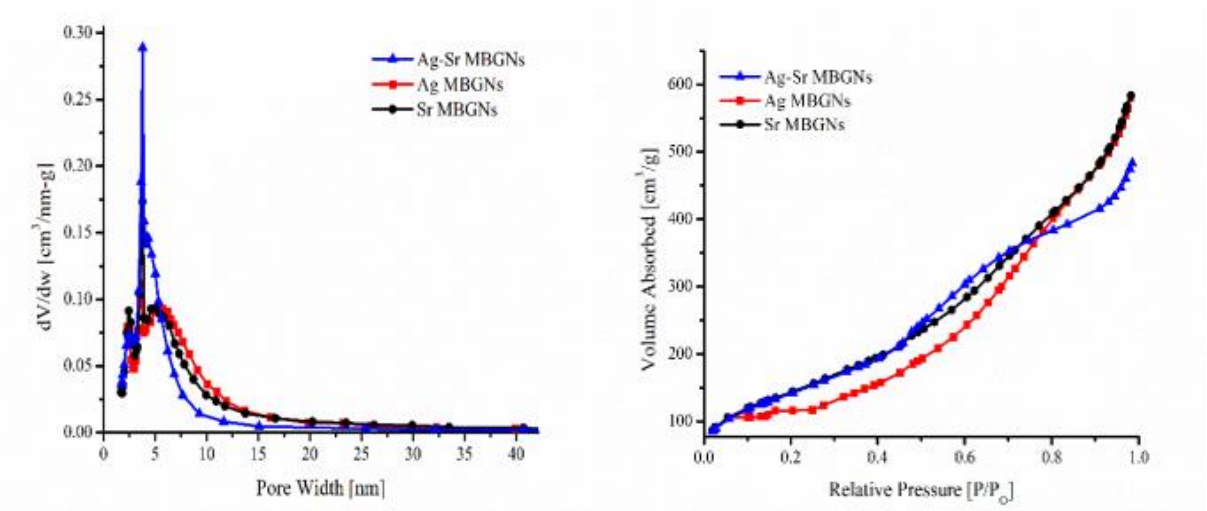


Figure 3. Nitrogen adsorption-desorption isotherms of synthesized bioactive glass nanoparticles(left) and pore size distribution (right)

### 3.2. Compositional Analysis

The EDX analysis was conducted, to confirm the addition of Ag and Sr in MBGNs. Figure 4A represents the peaks of Ag and Sr which confirmed the substitution of Ag and Sr in MBGNs Figure 4B represents the qualitative elemental EDX analysis of the synthesized MBGNs prior to the substitution of Ag and Sr ions. It was observed that the Ca and Si peaks are present in MBGNs, which indicated the formation MBGNs [36]. The results of EDX analysis are in good qualitative agreement with the nominal composition of the synthesized MBGNs, as presented in Table 1.

Preprints (www.preprints.org) | NOT PEER-REVIEWED | Posted: 10 February 2021 doi:10.20944/preprints202102.0245.v1

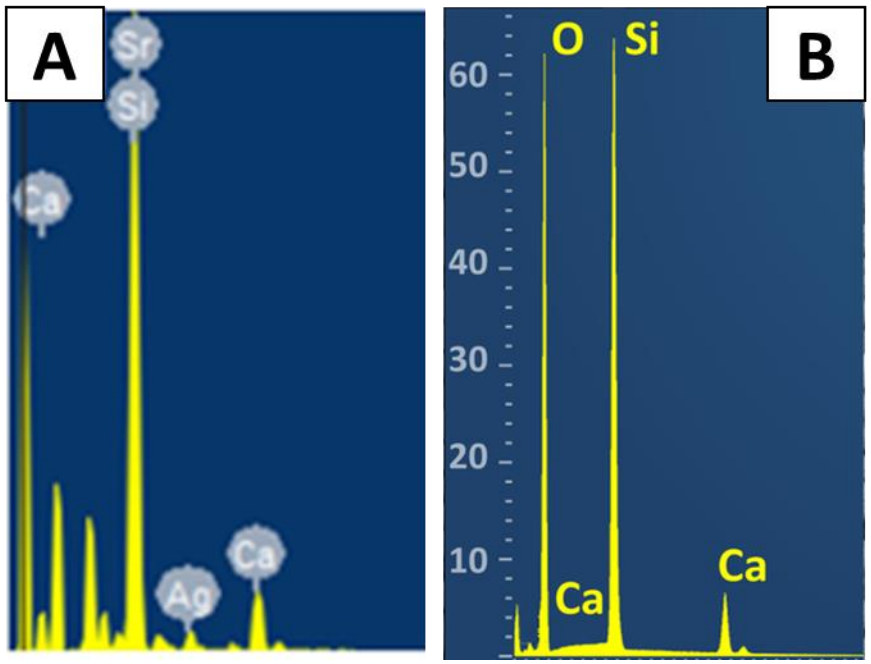


Figure 4. EDX analysis of the synthesized particles; (A) Ag-Sr MBGNs and (B) MBGNs

FTIR results depicted that no major difference occurs upon doping metallic precursors [36]. The molecular structure of as-synthesized Ag-Sr MBGNs and the effect of doping on a network of glass were studied by FTIR spectroscopy (Figure 5). The bands around 455 $cm^{-1}$ and 1067 $cm^{-1}$ can be assigned to Si–O–Si stretching and Si–O–Si rocking modes, respectively [37]. The broad band at 1200 to 1000 $cm^{-1}$ depicts Si-O-Si vibrations [38]. Intensity of non-bridging oxygen (NBO) peak observed at 799 $cm^{-1}$ for MBGNs in silica network [29].

Preprints (www.preprints.org) | NOT PEER-REVIEWED | Posted: 10 February 2021 doi:10.20944/preprints202102.0245.v1

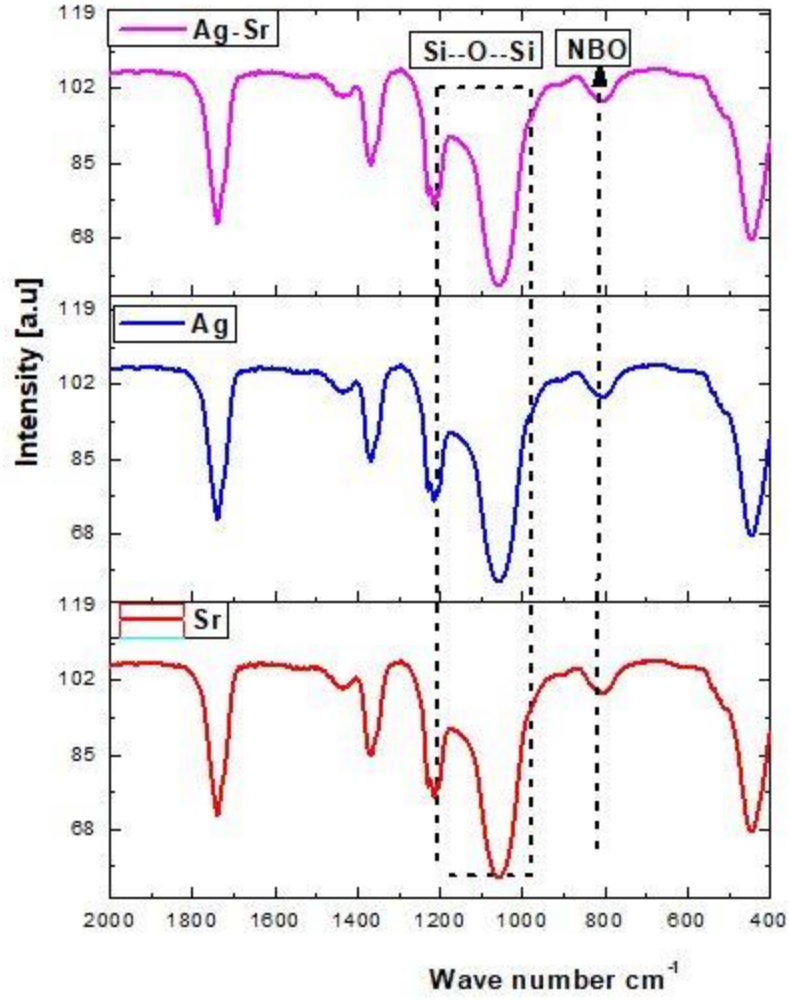


Figure 5 FTIR spectroscopy of Ag-Sr, Ag MBGNs, and Sr MBGNs.

The XRD diffraction pattern of as synthesized MBGNs, Ag MBGNs, Sr MBGNs, and Ag-Sr MBGNs confirmed the amorphous nature (broad peak at 2θ = 20°–32°) for all types of MBGNs, as shown in Figure 6 [39]. Furthermore, the diffraction pattern of Ag-Sr MBGNs shows no peaks ascribed to the silver and strontium, which suggests the incorporation of Ag and Sr into MBGNs as well as the chemical homogeneity of Ag-Sr containing MBGNs. It was concluded that Ag-Sr MBGNs was successfully synthesized using the microemulsion assisted sol–gel approach presented here with silver nitrate and strontium nitrate being an effective precursor for incorporating Ag and Sr into silica network of MBGNs.

Preprints (www.preprints.org) | NOT PEER-REVIEWED | Posted: 10 February 2021 doi:10.20944/preprints202102.0245.v1

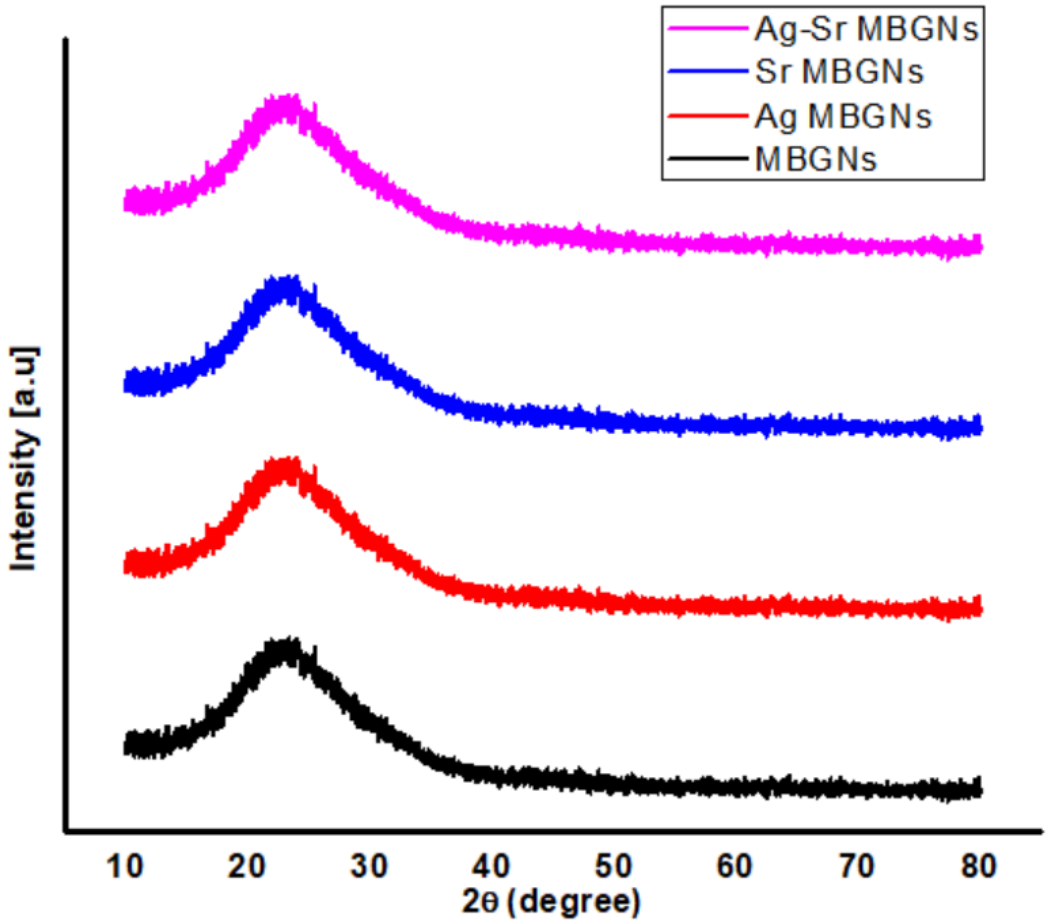


Figure 6. XRD patterns of Ag-Sr, Ag, Sr doped MBGNs.

### 3.3. Zeta potential

The zeta potential measurements of MBGNs, Ag MBGNs, Sr MBGNs, and Ag-Sr MBGNs were performed in ethanol, and the results are given in Table 2. It was deduced that silver and strontium ions changed the surface charge of MBGNs. Strontium substitution resulted in an increase in positive surface charge, while Ag substitution led to a decrease in surface charge. The reason is that strontium (electronegativity 0.95) is more electropositive compared to calcium (electronegativity 1.0), and therefore its substitution leads to an increase in surface charge [40]. Positive zeta potential increases the solubility of the nanoparticles and may lead to aggregation. However, it also promotes the adsorption of negatively charged proteins on the surface and improves the efficacy of imaging, gene transfer, and drug delivery [41]. Silver ion reduces the surface charge of MBGNs due to its high electronegativity (1.93) compared to calcium (1.0), which

Preprints (www.preprints.org) | NOT PEER-REVIEWED | Posted: 10 February 2021 doi:10.20944/preprints202102.0245.v1

facilitates the deposition of $Ca^{2+}$ ions on the surface and enhances the bioactivity [42].

**Table 2:** Zeta potential measurements for MBGNs, Ag MBGNs, Sr MBGNs and Ag-Sr MBGNs nanoparticles in pure ethanol.

| Particles | Zeta potential ± SD [mV] |
|---|---|
| HA | $22 \pm 3$ |
| Ag MBGNs | $15 \pm 2$ |
| Sr MBGNs | $34 \pm 3$ |
| Ag-Sr MBGNs | $17 \pm 2$ |

### 3.4. Ion-release Profile

The synthesized MBGNs was tracked for ion release study in order to understand the effect of ion release on the biological properties, for example, antibacterial activity, in-vitro bioactivity and cell biology. Figure 7A represents the release of Si and Ca ions from MBGNs. It was observed that Si showed a rapid release in all samples in the first 7 days, followed by a relatively slow release up to 21 days. $Ca^{+2}$ ions were released at a rapid rate from all types of MBGNs. However, the absolute release of Ca ions decreases with the increase in the incubation time. The release of Ca ions is beneficial for the osteo-conductive properties of the bioactive glasses. Figure 7B shows the release profile of Ag and Sr ions from co-substituted MBGNs under dynamic condition in SBF solution at 37 °C over a period of 21 days. A burst release of Ag ions was observed in the first 24 hours in Ag-Sr MBGNs and Ag MBGNs samples followed by a steady state release, indicating long-term sustained release, which will be beneficial for long-term antibacterial effect. Figure 7C shows the release profile of Si, Ca and Ag ions from the Ag MBGNs. We observed burst release of Ag ions during first week. Afterwards, the sustained release of Ag ions was observed. The ion release profile of Si, Ca, and Ag from Ag MBGNs was similar to the Ag- Sr MBGNs. Furthermore, the release of Sr, Si, and Ca from Sr MBGNs was similar to that of Ag-Sr MBGNs. Thus, it was concluded that the co-substitution of Ag and Sr did not affect the release of Si and Ca ions, which will be helpful in obtaining bioactive properties while keeping the antibacterial effect associated with the release of Ag ions.

Preprints (www.preprints.org) | NOT PEER-REVIEWED | Posted: 10 February 2021 doi:10.20944/preprints202102.0245.v1

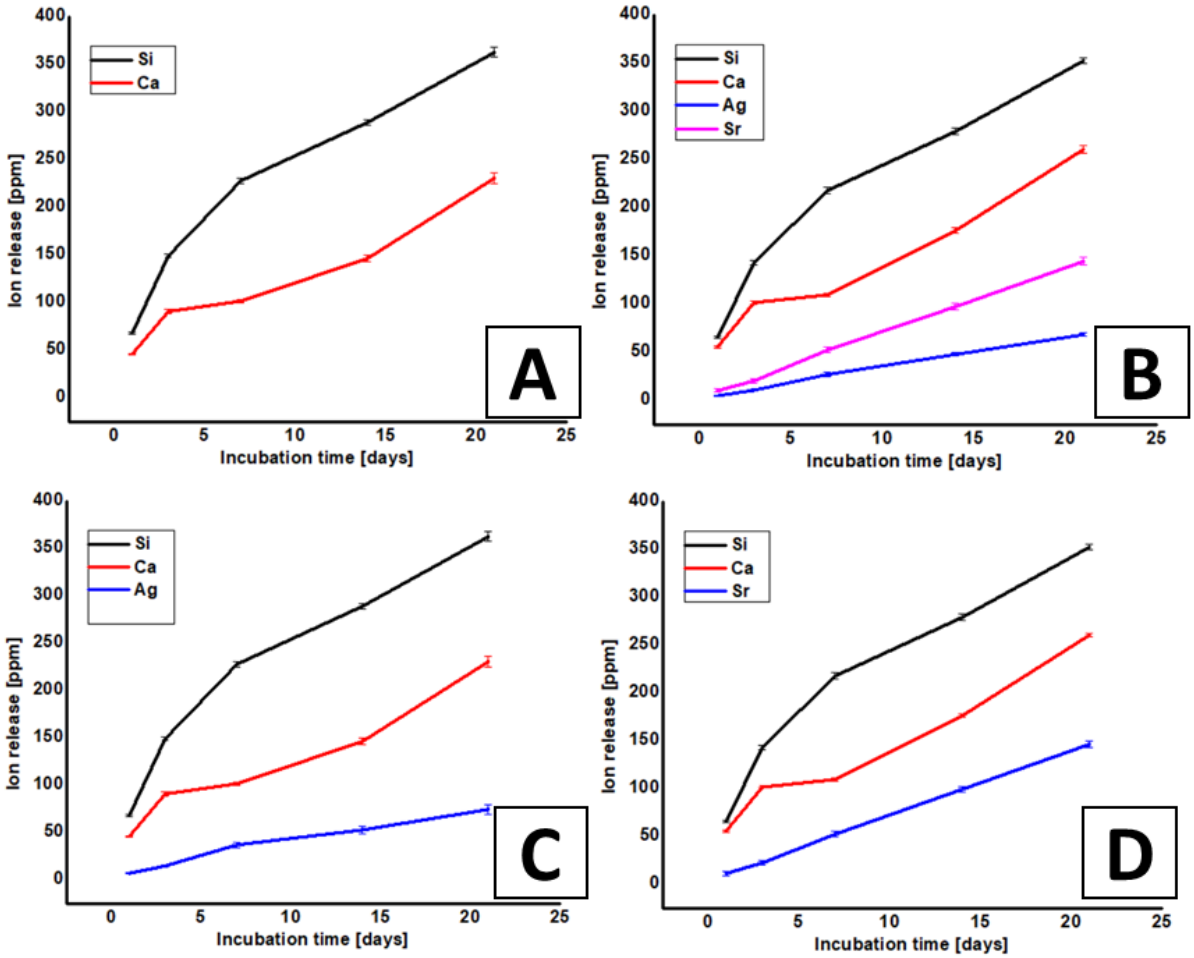


**Figure 7**: Absolute ion release profile of Si,Ca, Sr and Ag ions from Ag-Sr MBGNs samples immersed in SBF measured by using ICP (Eeach experiment was repeated 5 times and the mean values were reported with the standard deviation represented by the error bars in the figure)

The burst release of both ions (Ag, Sr) was observed from Ag-Sr MBGNs, which might be due to the concentration gradient between the particles and physiological solution. Ag ions released in the physiological medium play an important role in the antibacterial activity. The antibacterial properties (discussed in section 3.5) of the synthesized MBGNs were in good agreement with ion release data. Ag ions released from Ag-Sr MBGNs samples were within the concentration range of 2–48 ppm, which has been proven to induce significant antibacterial properties against Gram-positive and Gram-negative bacterial strains [43]. The sustained release of Sr ions will be beneficial for in-vitro bioactivity [44].

Preprints (www.preprints.org) | NOT PEER-REVIEWED | Posted: 10 February 2021 doi:10.20944/preprints202102.0245.v1

### 3.5. Antibacterial Study (Turbidity test)

To investigate the antimicrobial effect of synthesized nanoparticles of different compositions a turbidity test was done. The change in $OD_{600}$ after 1, 2, 3, 4, 6 and 24 hours of incubation is presented in Table 3. It was observed that the measured value $OD_{600}$ for the Ag-Sr MBGNs and Ag MBGNs show a strong decrease after 6 h of incubation compared to the control samples (MBGNs and Sr MBGNs). Since Ag ions released in a substantial amount after 6 h of incubation, which resist the growth of E. Coli and S. carnasous. After 24 h of incubation, the cumulative release of Ag ions from Ag MBGNs and Ag-Sr MBGNs was sufficient to completely hinder the growth of E. Coli and S.carnasous. Moreover, it was observed that the control samples allowed the growth E. Coli and S. carnasous after 24 hours of incubation. Thus, it can be concluded that the Ag-Sr MBGNs and Ag MBGNs strongly retarded the growth of E. Coli cells [45].

Table 3. Results of the turbidity test ($OD_{600}$) carried out on MBGNs, Ag-Sr MBGNs, Ag MBGNs, and Sr MBGNs after 1, 2, 3, 4, 6, and 24 hours of incubation (each experiment is repeated thrice and the mean value is reported along with the standard deviation).

| Time (h) | MBGNs | Ag-Sr MBGNs | Ag MBGNs | Sr MBGNs |
|---|---|---|---|---|
| 1 | 0.010±0.002 | 0.020±0.003 | 0.025±0.004 | 0.010±0.005 |
| 2 | 0.010±0.003 | 0.030±0.005 | 0.025±0.008 | 0.020±0.007 |
| 3 | 0.040±0.005 | 0.040±0.005 | 0.030±0.007 | 0.055±0.009 |
| 4 | 0.050±0.007 | 0.010±0.002 | 0.008±0.003 | 0.065±0.012 |
| 6 | 0.070±0.008 | 0.005±0.001 | 0.003±0.001 | 0.090±0.032 |
| 24 | 0.190±0.010 | 0±0 | 0±0 | 0.205±0.12 |

### 3.6. Disc diffusion test (inhibition halo method)

The antibacterial properties of the Ag-Sr MBGNs and MBGNs was also investigated by the disc diffusion method (Figure 8) to further validate the antibacterial results. The antibacterial effect was tracked against Gram-negative (E. coli) and Gram-positive (S. carnosus) bacteria. The growth of E.coli and S. carnosus was prominent on the reference and pure MBGNs sample after 24 hours of incubation. The growth for the both types of bacteria was strongly inhibited by the Ag-Sr MBGNs samples. Figure 8 shows that the zone of inhibition developed across MBGNs sample

Preprints (www.preprints.org) | NOT PEER-REVIEWED | Posted: 10 February 2021 doi:10.20944/preprints202102.0245.v1

against S. carnosus and E. coli. The strong antibacterial effect associated with the Ag-Sr MBGNs was due to the release of silver ions (as shown in Figure 7). The silver ions interact with nucleic acids and they interact preferentially with the bases in DNA thus, inhibiting the DNA replication activity and eventually leading to the death of bacteria. Furthermore, Ag in an ionic form is highly reactive (generation of reactive oxygen species) and can rupture the walls of bacteria and leading to the death of bacteria cells [1,11].

In the current study, Ag was successfully doped in the network of MBGNs (Figure 6) and the Ag was released in an ionic form rather than the particulate form. Ag in the form of particles is toxic to the osteoblast cells. However, the controlled release of silver ions <100 ppm (as the case in present study see Figure 7) provided potent antibacterial effect against wide spectrum of bacteria. The release of silver ions was <100 ppm, which is below the cytotoxic limit of Ag [10,46].

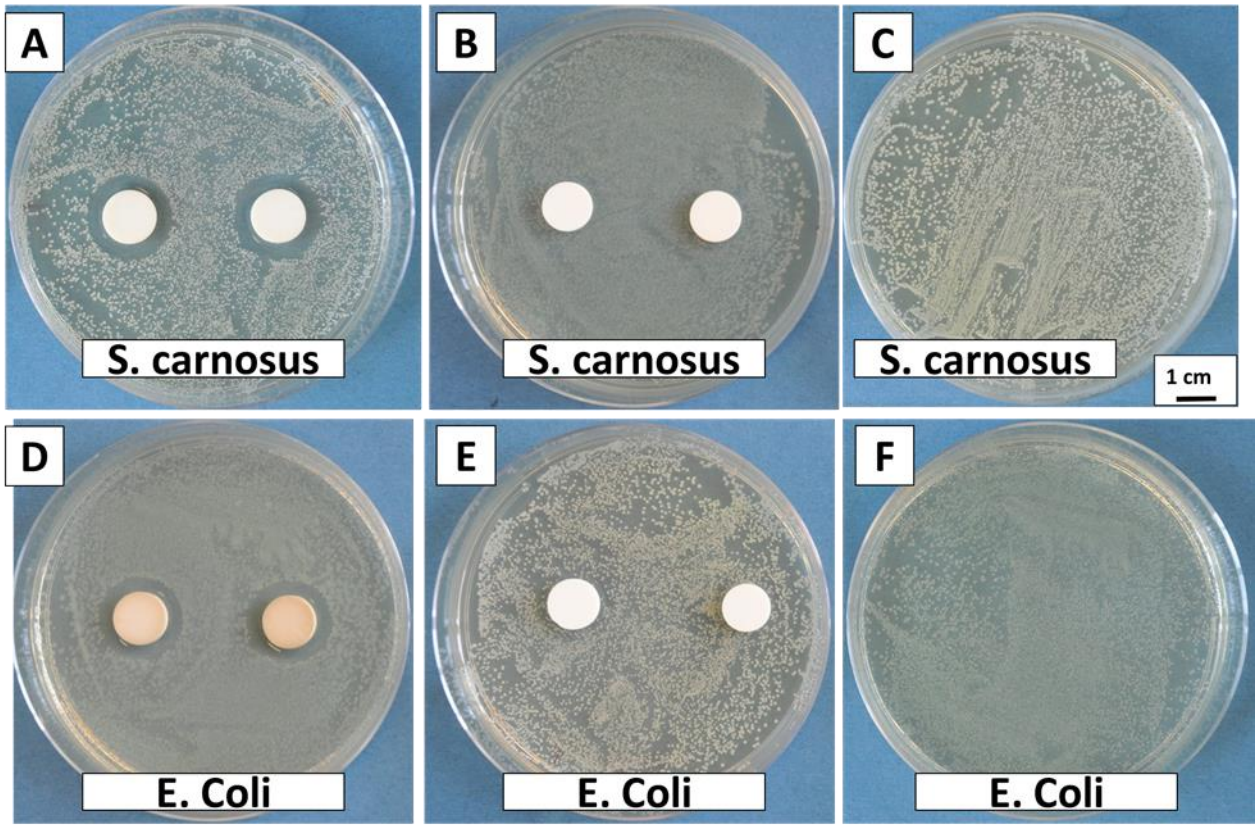


Figure 8. Inhibition halo tests with S. carnosus for (A) Ag-Sr MBGNs, (B) MBGNs, (C) reference sample and with E. coli for (D) Ag-Sr MBGNs, (E) MBGNs, (F) reference sample.

Preprints (www.preprints.org) | NOT PEER-REVIEWED | Posted: 10 February 2021 doi:10.20944/preprints202102.0245.v1

The cytotoxicity of Ag doped MBGNs depends on the concentration of Ag in MBGNs and the release profile of Ag [29,47]. However, the cytotoxic effect associated with the release of Ag ions can be copedby the addition of Sr ions. In our previous study, we have shown that the toxic effect of Ag can be minimized by the co-substitution of Sr and Mn along with the Ag [1,6,22]. Therefore, this study presents new frontier in the field of biomedical materials by the use of co-substituted Ag and Sr ions. The co-substitution of Ag and Sr is challenging task because Ag tends to oxidize readily and form AgO. However, in this study we developed MBGNs doped with Ag in its pure form (XRD results indicate no crystalline peak of silver oxide) due to which it was possible to release silver in an ionic form rather than particulate form [10].

### 3.7. In-vitro bioactivity analysis

Bioactivity is one of the most desired attributes for bone tissue engineering (BTE). The ability of the coating to form a bond with the bone is crucial for an implant [48]. Figure 9 represents the EDX analysis of the Ag-Sr MBGNs after immersion in SBF. The decrease in the intensity of Si peak over the immersion time in SBF may indicates the degradation of Ag-Sr MBGNs or the formation of thick layer of hydroxyapatite (HA)[5]. Moreover, it was observed that the intensity of calcium and phosphate peaks increased over the incubation time which indicates the formation of HA crystals on the surface of the Ag-Sr MBGNs [49]. In-vitro bioactivity of pure MBGNs is illustrated in our previous studies [27]. Furthermore, the toxic effect of Ag MBGNs on the bioactivity was also illustrated in our previous studies [1][6].

Preprints (www.preprints.org) | NOT PEER-REVIEWED | Posted: 10 February 2021 doi:10.20944/preprints202102.0245.v1

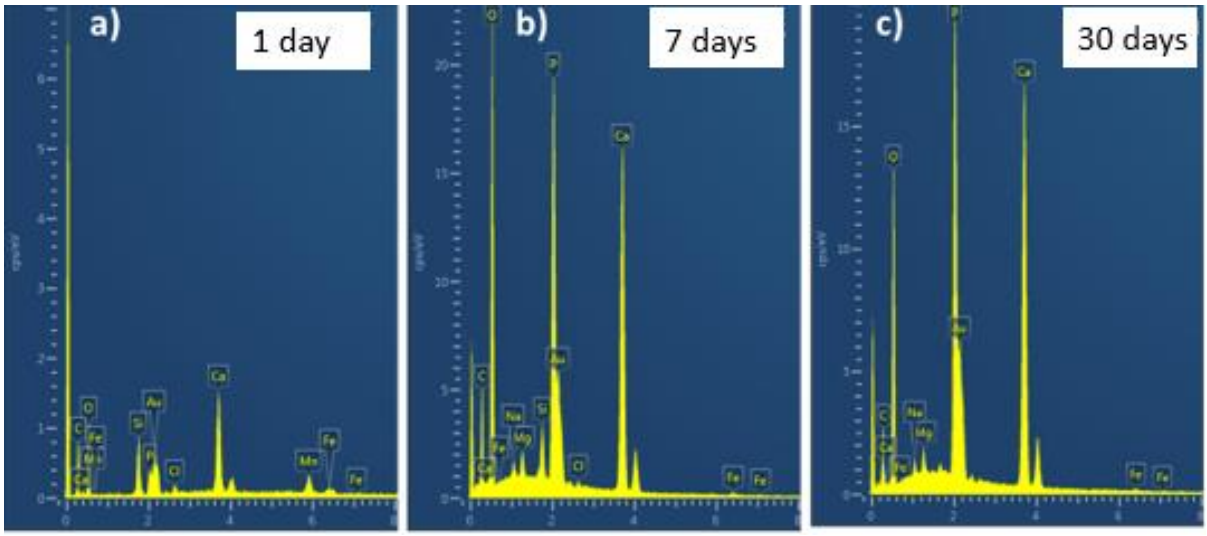


Figure 9. EDX analysis of synthesized Ag-Sr MBGNs after immersion in SBF (A) 1 day (B) 3 days and (C) 1 month

Figure 10 shows the SEM images of the synthesized Ag-Sr MBGNs after immersion in SBF. Figure 10 depicts the change in the morphology of nanoparticles. After 7 days of immersion in SBF nanostructure and porous HA crystals formed on the surface of the particles. It was further observed that the plate-like HA crystals form on the surface of incubated (HA). The plate-like structure indicated the calcium enriched apatite crystals [12].

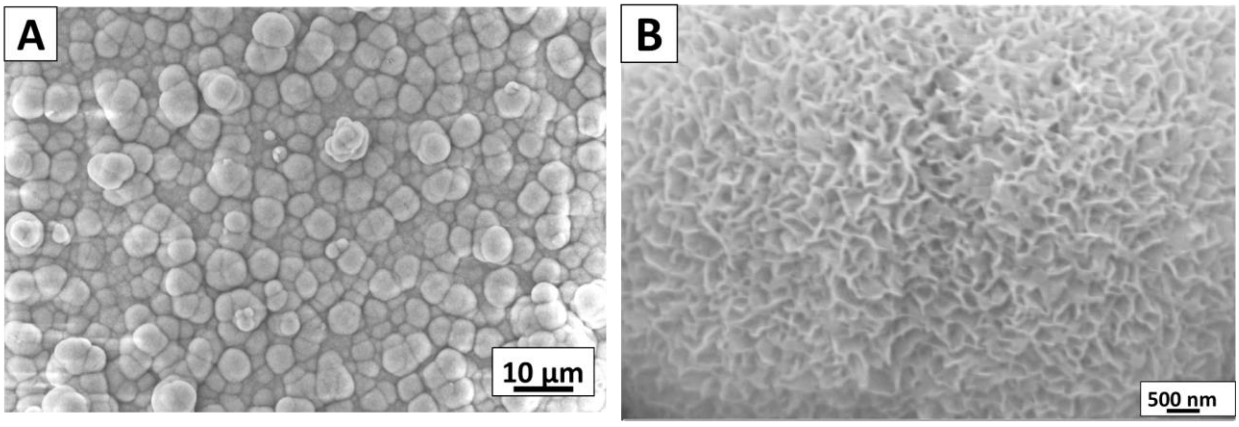


Figure 10. SEM images of Ag-Sr MBGNs pellets after immersion in SBF for 7 days, (A) low magnification image, (B) Higher magnification image

Preprints (www.preprints.org) | NOT PEER-REVIEWED | Posted: 10 February 2021 doi:10.20944/preprints202102.0245.v1

Studies show that bone reformation is pH sensitive. During bone remodeling around the border of osteoclast, pH is 4.0 and the pH of surrounding body fluid is 7.4 [50,51]. Moreover, it is known that the physiological environment of initial fracture hematoma is acidic, during healing it becomes alkaline which aids bone differentiation [52]. To study the pH changes, Ag-Sr MBGNs samples were immersed in SBF and then incubated. SBF solution was changed after every 3 days and pH was checked initially on the $7^{th}$,$14^{th,}$ and $21^{st}$ days. Figure 11 shows that the pH became slightly basic as the immersion time increases which aids bone differentiation as mentioned earlier. The overall curve progression is stable, except for a few midterm fluctuations.

On the basis of in-vitro bioactivity and antibacterial studies it was inferred that the Ag-Sr MBGNs provided potent antibacterial effect while maintaining the typical bioactivity associated with the MBGNs. According to [47] Ag may affect the in-vitro bioactivity of the MBGNs. Thus, the addition of Sr improves the in-vitro bioactivity and provided antibacterial effect due to the Ag doping.

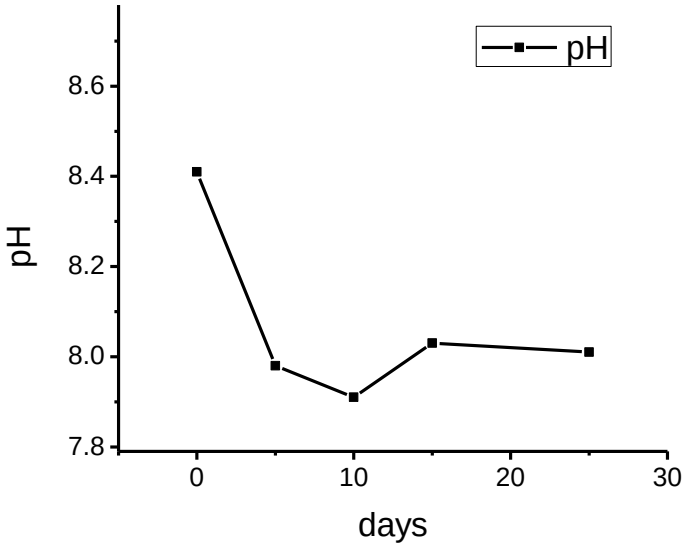


Figure 11. The difference in pH-value of SBF after immersion of Ag-Sr MBGNs. pH measured at different time points from 0 - 21 days

 doi:10.20944/preprints202102.0245.v1

## 4. Conclusions

In this study we synthesized Ag-doped, Sr doped, and Ag-Sr doped MBGNs via modified Stöber method and sol-gel process. SEM images confirmed the spherical morphology of all the synthesized particles. BET results confirmed the mesoporous nature of all the synthesized MBGNs. It was deduced that the addition of metallic ions did not affect the morphology of MBGNs. Furthermore, XRD results confirmed the doping of Ag and Sr in the silica network of MBGNs. The XRD patterns confirmed the amorphous nature of the synthesized MBGNs with all the different concentrations. The release of Ag and Sr ions was tracked by the ICP studies. The results confirmed that during first day of incubation Ag and Sr showed a burst release. However, with the increase in incubation time Ag and Sr was released in a sustained manned thus, providing long-term therapeutic effect. The Controlled release of Ag provided a potent antibacterial effect while the release of Sr ions improve the in-vitro bioactivity. The peculiar morphological features of the synthesized Ag-Sr MBGNs and the feasibility of functionalizing these MBGNs with active ions or biomolecules suggest that the synthesized MBGNs based on $SiO_2$-CaO in this study is a promising material for biomedical applications including bone regeneration and wound cure.

## 5. References

1. Aqib, R.; Kiani, S.; Bano, S.; wadood, A.; Ur Rehman, M.A. Ag-Sr Doped Mesoporous Bioactive Glass Nanoparticles Loaded Chitosan/Gelatin Coating for Orthopedic Implants. *Int. J. Appl. Ceram. Technol.*

2. Gao, C.; Peng, S.; Feng, P.; Shuai, C. Bone biomaterials and interactions with stem cells. *Bone Res.* **2017**, *5*, 1–33, doi:10.1038/boneres.2017.59.

3. Navarro, M.; Michiardi, A.; Castaño, O.; Planell, J.A.; Interface, J.R.S.; Navarro, M.; Michiardi, A.; Castan, O. Biomaterials in orthopaedics Biomaterials in orthopaedics. **2008**, 1137–1158, doi:10.1098/rsif.2008.0151.

4. Trampuz, A.; Osmon, D.R.; Hanssen, A.D.; Steckelberg, J.M.; Patel, R. Molecular and antibiofilm approaches to prosthetic joint infection. *Clin. Orthop. Relat. Res.* **2003**, 69–88, doi:10.1097/01.blo.0000087324.60612.93.

5. Ur Rehman, M.A.; Bastan, F.E.; Nawaz, A.; Nawaz, Q.; Wadood, A. Electrophoretic deposition of PEEK/bioactive glass composite coatings on stainless steel for orthopedic applications: an optimization for in vitro bioactivity and adhesion strength. *Int. J. Adv. Manuf. Technol.* **2020**, *108*, 1849–1862, doi:10.1007/s00170-020-05456-x.

6. Nawaz, A.; Bano, S.S.; Yasir, M.; Wadood, A.; Ur Rehman, M.A.; Rehman, M.A.U. Ag and Mn-doped mesoporous bioactive glass nanoparticles incorporated into the chitosan/gelatin coatings deposited on PEEK/bioactive glass layers for favorable osteogenic differentiation and antibacterial activity. *Mater. Adv.* **2020**, *1*, 1273–1284, doi:10.1039/D0MA00325E.

7. Ercan, B.; Kummer, K.M.; Tarquinio, K.M.; Webster, T.J. Decreased Staphylococcus aureus biofilm growth on anodized nanotubular titanium and the effect of electrical stimulation. *Acta Biomater.* **2011**, *7*, 3003–3012, doi:10.1016/j.actbio.2011.04.002.

8. Postler, A.; Lützner, C.; Beyer, F.; Tille, E.; Lützner, J. Analysis of Total Knee Arthroplasty revision causes. **2018**, 1–6.

9. Khatoon, Z.; Mctiernan, C.D.; Suuronen, E.J.; Mah, T. Bacterial bio fi lm formation on implantable devices and approaches to its treatment and prevention. *Heliyon* **2018**, e01067, doi:10.1016/j.heliyon.2018.e01067.

10. Ur Rehman, M.A.; Ferraris, S.; Goldmann, W.H.; Perero, S.; Bastan, F.E.; Nawaz, Q.; Confiengo, G.G. Di; Ferraris, M.; Boccaccini, A.R. Antibacterial and Bioactive Coatings Based on Radio Frequency Co-Sputtering of Silver Nanocluster-Silica Coatings on PEEK/Bioactive Glass Layers Obtained by Electrophoretic Deposition. *ACS Appl. Mater. Interfaces* **2017**, *9*, 32489–32497, doi:10.1021/acsami.7b08646.

11. Saleem, O.; Wahaj, M.; Akhtar, M.A.; Ur Rehman, M.A. Fabrication and Characterization of Ag–Sr-Substituted Hydroxyapatite/Chitosan Coatings Deposited via Electrophoretic Deposition: A Design of Experiment Study. *ACS Omega* **2020**, *5*, 22984–22992, doi:10.1021/acsomega.0c02582.

12. Taylor, P.; Ribeiro, M.; Monteiro, F.J.; Ferraz, M.P.; Ribeiro, M.; Monteiro, F.J.; Ferraz, M.P. studying bacterial-material interactions Infection of orthopedic implants with

emphasis on bacterial adhesion process and techniques used in studying bacterial-material interactions. 37–41, doi:10.4161/biom.22905.

13. Hench, L.L. The story of Bioglass®. *J. Mater. Sci. Mater. Med.* **2006**, *17*, 967–978, doi:10.1007/s10856-006-0432-z.

14. Zro, Z. Biomaterials generations Bioceramic materials.

15. Atiq, M.; Rehman, U.; Azeem, M.; Schubert, D.W.; Boccaccini, A.R.; Rehman, M.A.U.; Munawar, M.A.; Schubert, D.W.; Boccaccini, A.R. Electrophoretic deposition of chitosan/gelatin/bioactive glass composite coatings on 316L stainless steel: A design of experiment study. *Surf. Coatings Technol.* **2019**, *358*, 976–986, doi:10.1016/j.surfcoat.2018.12.013.

16. Leena, R.S.; Vairamani, M.; Selvamurugan, N. Alginate/Gelatin scaffolds incorporated with Silibinin-loaded Chitosan nanoparticles for bone formation in vitro. *Colloids Surfaces B Biointerfaces* **2017**, *158*, doi:10.1016/j.colsurfb.2017.06.048.

17. Nair, L.S.; Laurencin, C.T. Biodegradable polymers as biomaterials. *Prog. Polym. Sci.* **2007**, *32*, 762–798, doi:10.1016/j.progpolymsci.2007.05.017.

18. Cormack, A.N.; Tilocca, A. Structure and biological activity of glasses and ceramics. *Philos. Trans. R. Soc. A Math. Phys. Eng. Sci.* **2012**, *370*, 1271–1280, doi:10.1098/rsta.2011.0371.

19. Wu, C.; Chang, J. Mesoporous bioactive glasses: Structure characteristics, drug/growth factor delivery and bone regeneration application. *Interface Focus* **2012**, *2*, 292–306, doi:10.1098/rsfs.2011.0121.

20. Yan, X.; Huang, X.; Yu, C.; Deng, H.; Wang, Y.; Zhang, Z.; Qiao, S.; Lu, G.; Zhao, D. The in-vitro bioactivity of mesoporous bioactive glasses. *Biomaterials* **2006**, *27*, 3396–3403, doi:10.1016/j.biomaterials.2006.01.043.

21. Westhauser, F.; Wilkesmann, S.; Nawaz, Q.; Hohenbild, F.; Rehder, F.; Saur, M.; Fellenberg, J.; Moghaddam, A.; Ali, M.S.; Peukert, W.; et al. Effect of manganese, zinc, and copper on the biological and osteogenic properties of mesoporous bioactive glass nanoparticles. *J. Biomed. Mater. Res. - Part A* **2020**, doi:10.1002/jbm.a.37136.

22. Nawaz, A.; Ur Rehman, M.A. Chitosan/gelatin-based bioactive and antibacterial coatings deposited via electrophoretic deposition. *J. Appl. Polym. Sci.* **2021**, *138*, 50220, doi:https://doi.org/10.1002/app.50220.

23. Boccaccini, F.W. and F.R. and S.D. and E.K. and A.M. and K.Z. and A.R. Ionic dissolution products of Cerium-doped bioactive glass nanoparticles promote cellular osteogenic differentiation and extracellular matrix formation of human bone marrow derived mesenchymal stromal cells. *Biomed. Mater.* **2020**.

24. Zheng, K.; Sui, B.; Ilyas, K.; Boccaccini, A.R. Porous bioactive glass micro- and nanospheres with controlled morphology: developments, properties and emerging biomedical applications. *Mater. Horizons* **2021**, doi:10.1039/d0mh01498b.

25. Westhauser, F.; Wilkesmann, S.; Nawaz, Q.; Schmitz, S.I.; Moghaddam, A.; Boccaccini, A.R. Osteogenic properties of manganese-doped mesoporous bioactive glass nanoparticles. *J. Biomed. Mater. Res. Part A* **2020**, *n/a*, doi:10.1002/jbm.a.36945.

26. Nawaz, Q.; Fuentes-Chandía, M.; Tharmalingam, V.; Rehman, M.A.U.; Leal-Egaña, A.; Boccaccini, A.R. Silibinin releasing mesoporous bioactive glass nanoparticles with potential for breast cancer therapy. *Ceram. Int.* **2020**.

27. Nawaz, Q.; Atiq, M.; Rehman, U.; Burkovski, A.; Schmidt, J.; Beltrán, A.M.; Shahid, A.; Alber, N.K.; Peukert, W.; Boccaccini, A.R.; et al. Synthesis and characterization of manganese containing mesoporous bioactive glass nanoparticles for biomedical applications. *J. Mater. Sci. Mater. Med.* **2018**, *5*, doi:10.1007/s10856-018-6070-4.

28. Li, W.; Zhao, D. Extension of the stöber method to construct mesoporous SiO2 and TiO2 shells for uniform multifunctional core-shell structures. *Adv. Mater.* **2013**, *25*, 142–149, doi:10.1002/adma.201203547.

29. Kozon, D.; Zheng, K.; Boccardi, E.; Liu, Y.; Liverani, L.; Boccaccini, A.R. Synthesis of monodispersed Ag-doped bioactive glass nanoparticles via surface modification. *Materials (Basel).* **2016**, *9*, doi:10.3390/ma9040225.

30. Bellucci, D.; Sola, A.; Cacciotti, I.; Bartoli, C.; Gazzarri, M.; Bianco, A.; Chiellini, F.; Cannillo, V. Mg- and / or Sr-doped tricalcium phosphate / bioactive glass composites :

Synthesis , microstructure and biological responsiveness. *Mater. Sci. Eng. C* **2014**, *42*, 312–324, doi:10.1016/j.msec.2014.05.047.

31. Virk, R.S.; Atiq, M.; Rehman, U.; Munawar, M.A.; Schubert, D.W.; Goldmann, W.H.; Dusza, J.; Boccaccini, A.R. Curcumin-Containing Orthopedic Implant Coatings Deposited on Poly-Ether-Ether-Ketone/Bioactive Glass/Hexagonal Boron Nitride Layers by Electrophoretic Deposition. *Coatings* **2019**, *9*.

32. Tabia, Z.; Akhtach, S.; Mabrouk, K. El; Bricha, M.; Nouneh, K.; Ballamurugan, A. Tantalum doped SiO2-CaO-P2O5based bioactive glasses: Investigation of in vitro bioactivity and antibacterial activities. *Biomed. Glas.* **2020**, *6*, 10–22, doi:10.1515/bglass-2020-0002.

33. Kokubo, T.; Takadama, H. How useful is SBF in predicting in vivo bone bioactivity? *Biomaterials* **2006**, *27*, 2907–2915, doi:10.1016/j.biomaterials.2006.01.017.

34. Greasley, S.L.; Page, S.J.; Sirovica, S.; Chen, S.; Martin, R.A.; Riveiro, A.; Hanna, J. V.; Porter, A.E.; Jones, J.R. Controlling particle size in the Stöber process and incorporation of calcium. *J. Colloid Interface Sci.* **2016**, *469*, 213–223, doi:10.1016/j.jcis.2016.01.065.

35. Wu, C.; Fan, W.; Chang, J. Functional mesoporous bioactive glass nanospheres: Synthesis, high loading efficiency, controllable delivery of doxorubicin and inhibitory effect on bone cancer cells. *J. Mater. Chem. B* **2013**, *1*, 2710–2718, doi:10.1039/c3tb20275e.

36. Cacciotti, I.; Lombardi, M.; Bianco, A.; Ravaglioli, A.; Montanaro, L. Sol-gel derived 45S5 bioglass: Synthesis, microstructural evolution and thermal behaviour. *J. Mater. Sci. Mater. Med.* **2012**, *23*, 1849–1866, doi:10.1007/s10856-012-4667-6.

37. Hoppe, A.; Meszaros, R.; Stähli, C.; Romeis, S.; Schmidt, J.; Peukert, W.; Marelli, B.; Nazhat, S.N.; Wondraczek, L.; Lao, J.; et al. In vitro reactivity of Cu doped 45S5 Bioglass® derived scaffolds for bone tissue engineering. *J. Mater. Chem. B* **2013**, *1*, 5659, doi:10.1039/c3tb21007c.

38. Zheng, K.; Dai, X.; Lu, M.; Hüser, N.; Taccardi, N.; Boccaccini, A.R. Synthesis of copper-containing bioactive glass nanoparticles using a modified Stöber method for

biomedical applications. *Colloids Surfaces B Biointerfaces* **2017**, *150*, 159–167, doi:10.1016/j.colsurfb.2016.11.016.

39. Zheng, K.; Fan, Y.; Torre, E.; Balasubramanian, P.; Taccardi, N.; Cassinelli, C.; Morra, M.; Iviglia, G.; Boccaccini, A.R. Incorporation of Boron in Mesoporous Bioactive Glass Nanoparticles Reduces Inflammatory Response and Delays Osteogenic Differentiation. *Part. Part. Syst. Charact.* **2020**, 2000054.

40. Hanifi, A.; Fathi, M.H.; Mir Mohammad Sadeghi, H. Effect of strontium ions substitution on gene delivery related properties of calcium phosphate nanoparticles. *J. Mater. Sci. Mater. Med.* **2010**, *21*, 2601–2609, doi:10.1007/s10856-010-4123-4.

41. Ravi, N.D.; Balu, R.; Sampath Kumar, T.S. Strontium-substituted calcium deficient hydroxyapatite nanoparticles: Synthesis, characterization, and antibacterial properties. *J. Am. Ceram. Soc.* **2012**, *95*, 2700–2708, doi:10.1111/j.1551-2916.2012.05262.x.

42. Qiu, Z.Y.; Noh, I.S.; Zhang, S.M. Silicate-doped hydroxyapatite and its promotive effect on bone mineralization. *Front. Mater. Sci.* 2013.

43. Uskoković, V.; Iyer, M.A.; Wu, V.M. One ion to rule them all: the combined antibacterial, osteoinductive and anticancer properties of selenite-incorporated hydroxyapatite. *J. Mater. Chem. B* **2017**, *5*, 1430–1445, doi:10.1039/C6TB03387C.

44. Erdem Bastan, F.; Ur Rehman, M.A.; Ustel, F. Thermo-physical insights into a series of strontium substituted hydroxyapatite. *Mater. Chem. Phys.* **2021**, *258*, 123910, doi:https://doi.org/10.1016/j.matchemphys.2020.123910.

45. Simchi, A.; Tamjid, E.; Pishbin, F.; Boccaccini, A.R. Recent progress in inorganic and composite coatings with bactericidal capability for orthopaedic applications. *Nanomedicine Nanotechnology, Biol. Med.* **2011**, *7*, 22–39, doi:10.1016/j.nano.2010.10.005.

46. Nawaz, Q.; Fastner, S.; Rehman, M.A.U.; Ferraris, S.; Perero, S.; di Confiengo, G.G.; Yavuz, E.; Ferraris, M.; Boccaccini, A.R. Multifunctional stratified composite coatings by electrophoretic deposition and RF co-sputtering for orthopaedic implants. *J. Mater. Sci.* **2021**, doi:10.1007/s10853-020-05725-w.

47. El-Rashidy, A.A.; Waly, G.; Gad, A.; Hashem, A.A.; Balasubramanian, P.; Kaya, S.; Boccaccini, A.R.; Sami, I. Preparation and in vitro characterization of silver-doped bioactive glass nanoparticles fabricated using a sol-gel process and modified Stöber method. *J. Non. Cryst. Solids* **2018**, *483*, 26–36, doi:https://doi.org/10.1016/j.jnoncrysol.2017.12.044.

48. Balamurugan, A.; Balossier, G.; Kannan, S.; Rajeswari, S. Elaboration of sol-gel derived apatite films on surgical grade stainless steel for biomedical applications. *Mater. Lett.* **2006**, *60*, 2288–2293, doi:10.1016/j.matlet.2005.12.126.

49. Ahmed, Y.; Ur Rehman, M.A.; Rehman, M.A.U. Improvement in the surface properties of stainless steel via zein/hydroxyapatite composite coatings for biomedical applications. *Surfaces and Interfaces* **2020**, *20*, 100589, doi:https://doi.org/10.1016/j.surfin.2020.100589.

50. Hollinger, J.; Wong, M.E.K. The integrated processes of hard tissue regeneration with special emphasis on fracture healing. *Oral Surgery, Oral Med. Oral Pathol. Oral Radiol. Endodontology* **1996**, *82*, 594–606.

51. Baron, R. Molecular mechanisms of bone resorption An update. *Acta Orthop. Scand.* **1995**, *66*, 66–70.

52. Baron, R.; Neff, L.; Louvard, D.; Courtoy, P.J. Cell-mediated extracellular acidification and bone resorption: evidence for a low pH in resorbing lacunae and localization of a 100-kD lysosomal membrane protein at the osteoclast ruffled border. *J. Cell Biol.* **1985**, *101*, 2210–2222.